STRUCTURAL BEHAVIOR OF PULTRUDED GFRP PROFILES

EXPERIMENTAL STUDY AND NUMERICAL MODELING

Manuel Mendes Correia

Department of Civil Engineering, Arquitecture and Georesources, Instituto Superior Técnico, Technical University of Lisbon, Av. Rovisco Pais, 1049-001 Lisbon – Portugal

February 2012

ABSTRACT: The design of GFRP pultruded profiles is limited by deformations in service limit states (SLS) and by local and/or global buckling in ultimate limit states (ULS). This work focuses on the structural behavior of GFRP pultruded I-profiles, particularly on the local buckling behavior. Hence, experimental studies were conducted: (i) coupon tests; and (ii) full-scale tests on short columns and three-point and four-point bending tests on beams. Numerical models using the finite element method (FEM) were developed to analyze the profiles local buckling. Using these models, the influence of different cross-section shapes and members length on local buckling was evaluated.

KEYWORDS: GFRP, structural behavior, beam, column, experimental tests, numerical modeling, local buckling.

1. INTRODUCTION

Glass Fiber Reinforced Polymers (GFRP) are composite materials made of glass fiber reinforced polymer matrix. Due to their high durability and lightweight qualities, GFRP profiles are a valid option as structural members. However, they are governed by deformations (SLS) and global and/or local buckling (ULS).

Local buckling of GFRP profiles has been a matter of study for many researchers. Both experimental and numerical studies were developed in order to increase the knowledge about the material and the local buckling phenomenon. Bank and Yin [1] studied experimentally and numerically postbuckled failure on I-beams, Turvey and Zhang [2] studied the same issues, but in the scope of columns. Experimental tests and numerical simulations conducted by Kollár [3, 4] enabled the development of analytical calculations to obtain the critical stress.

This work focuses on the local buckling phenomenon of E-glass/polyester pultruded I-profiles produced by Alto Pultrudidos (Figure 1). Table 1 shows the main geometrical properties of these I-profiles, used in the experimental tests.

Two different experimental studies were developed aiming to characterize the mechanical and structural behavior of GFRP pultruded I-profiles: (i) coupon tests in order to determine the GFRP's mechanical properties; (ii) full-scale tests of columns and beams, which provided data to analyze local buckling behavior, namely the determination of the buckling loads and collapse loads.

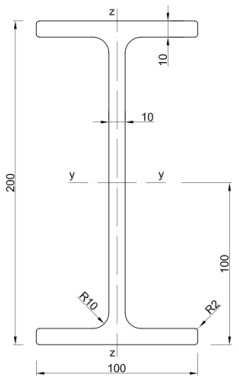

Figure 1 – I-profile cross-section (unit: mm).

Table 1
Geometrical properties of I-profiles.

A (mm^2)	3879.0
$A_{v,y}$ (mm^2)	2000.0
$A_{v,z}$ (mm^2)	1666.7
I_{yy} (mm^4)	2.353×10^7
I_{zz} (mm^4)	1.670×10^6
W_{yy} (mm^3)	2.353×10^5
W_{zz} (mm^3)	3.339×10^4

Numerical models using the shell finite element method (FEM) were developed based on mechanical and geometrical data obtained from the experimental tests. Column and beam models were developed to analyze the local buckling phenomenon. Calibration of those models was made on the basis of experimental full-scale data. Parametric studies were performed showing the influence of different cross-section shapes and structural members length on the buckling load of pultruded GFRP columns and beams.

2. LOCAL BUCKLING

Thin-walled GFRP profiles are sensitive to local buckling in compression parts due to the low elastic moduli and the high slenderness (width-to-thickness ratio) of plate elements (also called "walls"). In order to obtain the critical buckling stress, plate element analysis can be performed on the basis of the stiffness properties and boundary conditions.

Table 2 shows the stiffness properties for orthotropic plate elements, where E_x is the flexural longitudinal modulus, E_y is the flexural transversal modulus, G_{xy} is the shear modulus, ν_x is the longitudinal Poisson ratio and ν_y is the transversal Poisson ratio given by:

$$\nu_y = \nu_x \frac{E_y}{E_x} \tag{1}$$

Table 2
Stiffness properties for orthotropic plate elements.

	Stiffness	Expression	
D_x	flexural longitudinal direction	$\frac{E_x t^3}{12(1-\nu_x\nu_y)}$	(2)
D_y	flexural transversal direction	$\frac{E_y}{E_x} D_x$	(3)
D_{xy}	flexural transversal direction due to longitudinal bending	$\nu_y D_x$	(4)
D_s	shear stiffness	$\frac{G_{xy} t^3}{12}$	(5)

Figure 2 shows the cross-section of a generic I-profile, where b_f is the flange width, t_f the flange thickness, d_w the web depth and t_w the web thickness.

Figure 3 shows a plate model simulating the boundary conditions of a compressed (half) flange with a half-wave length (a). The plate is simply supported in one of the longitudinal edges (due to the presence of the web) and free in the other, and simply supported in both transversal edges due to the presence of other adjacent half-waves.

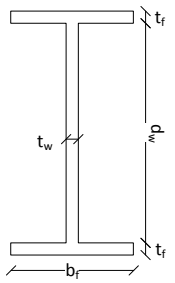

Figure 2 – I-profile generic cross-section.

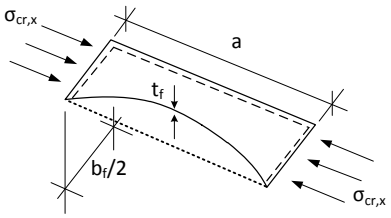

Figure 3 – Local buckling on a flange due to compression schematic.

Analytical calculations developed by Kollár, based on experimental tests and numerical simulations [3, 4], conducted to several equations for different types of longitudinal boundary conditions. For a wall with one free edge and one simply supported under uniform compression (typically a compressed flange), the critical stress is given by:

$$\sigma_{cr0,f}^{local} = \frac{4t_f^2}{b_f^2} G_{xy} \tag{6}$$

For a wall with two simply supported edges under uniform compression (typically a column web), the critical stress is given by:

$$\sigma_{cr0,w,c}^{local} = \frac{2\pi^2}{t_w d_w^2}\left(\sqrt{D_x D_y} + D_{xy} + 2D_s\right) \tag{7}$$

For a wall with two simply supported edges under linearly varying compression (typically a beam web), the critical stress is given by:

$$\sigma_{cr0,w,b}^{local} = \frac{\pi^2}{t_w d_w^2}\left(13{,}9\sqrt{D_x D_y} + 11{,}1D_{xy} + 22{,}2D_s\right) \tag{8}$$

Based on Kollár's method, starting from simply supported plate models in order to identify which wall will buckle first, the critical buckling stress can be obtain using a coefficient that takes into account the effect of edge restraint.

3. COUPON TESTS

In order to obtain stiffness and strength of the I-profiles material used in the experimental studies, mechanical characterization was carried out for both principal directions of the material (Figure 4). Thus, web and flanges coupons extracted from those profiles were tested to obtain elastic modulus and ultimate strength values.

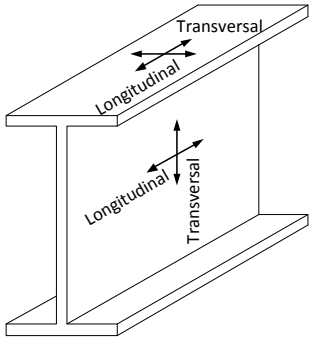

Figure 4 – Principal directions of I-profile materials.

Therefore, several coupon tests were conducted according with ISO and ASTM standard test methods: (i) compression (ASTM D695 [5]); (ii) tension (ISO 527 [6]); (iii) three-point bending (ISO 14125 [7]); and (iv) interlaminar shear (ASTM D2344 [8]). Other coupon tests were conducted aiming to obtain: (i) Poisson's ratio – tension coupon tests (ISO 527 [6]); and in-plane shear modulus – 10° off-axis tension coupon (ISO 527-5 according to [9]).

Flange and web mechanical properties were similar, showing reasonable homogeneity throughout the profile; hence, the material strength and stiffness results can be averaged and taken for the entire cross-section. Table 3 summarizes both elastic modulus and ultimate strength average results for flange and web coupons, and also Poisson ratio and shear modulus values. Linear elastic behav-

ior was observed for the load-displacement curves obtained from coupon tests. Different results obtained for longitudinal and transverse material principal directions indicate clear orthotropic behavior, as expected.

Table 3
Strength and stiffness properties of the material.

Test type	Principal material direction	Elastic modulus (GPa)	Ultimate strength (MPa)
Compression	Longitudinal ($\sigma_{cu,x}$)	30.27	412.99
	Transversal ($\sigma_{cu,y}$)	5.04	80.27
Tension	Longitudinal ($\sigma_{tu,x}$)	34.51	393.50
Bending	Longitudinal ($\sigma_{bu,x}$)	24.83	493.76
Interlaminar shear	Longitudinal (F_{SBS})	-	29.81
Poisson ratio	0.279	Shear modulus (GPa)	3.67

Figures 3 to 8 show coupon failure mode for each test described above.

4. FULL-SCALE TESTS

Strength and stiffness properties of GRFP members, on a full-scale level, may not be uniform within the cross-section due to the inhomogeneity and anisotropy of the material [10]. Thus, full-scale tests were conducted in order to obtain the member stiffnesses, such as bending stiffness (*EI*), axial stiffness (*EA*) and transverse shear stiffness (GkA_v), where *E* is the elastic modulus, *G* is the shear modulus, *I* is the inertia moment about the major-axis, *A* the cross-section area, A_v is the shear area and *k* the Timoshenko shear coefficient.

Therefore, five short columns were tested, as well as two beams, one subjected to three-point bending and another subjected to four-point bending. GFRP pultruded I-profiles produced by Alto Perfis Pultrudidos were used.

4.1. Short column tests

Aiming to obtain the axial stiffness, the buckling and ultimate loads, five 600 mm columns were tested (numbered C1 to C5). The columns ends were restrained from rotating about the major and minor bending axis by 30 mm thick epoxy resin solid blocks. Figure 11 shows the testing scheme used for short columns, and Figure 12 shows column C5 test setup.

The load was applied to the lower plate by a *Enerpac* hydraulic jack with 3000 kN load capacity and a maximum stroke of 400 mm; it was measured by means of a *Microtest* load cell with 3000 kN capacity. The deflections on the upper plate were measured by three *TML-10* displacement transducers (10 mm range and 0.01 mm precision). The lower plate deflections were measured by means of two *APEK-25* (25 mm range and 0.01 mm precision) and one *TML-25* (25 mm range and 0.01 mm precision) displacement transducers.

Figure 5 – Compression coupon test failure mode.

Figure 6 – Tension coupon test failure mode.

Figure 7 – Three-point bending coupon test failure mode.

Figure 8 – Interlaminar coupon test failure mode.

Figure 9 – Tension coupon test failure mode to obtain Poisson's ratio.

Figure 10 - 10° off-axis tension coupon test failure mode.

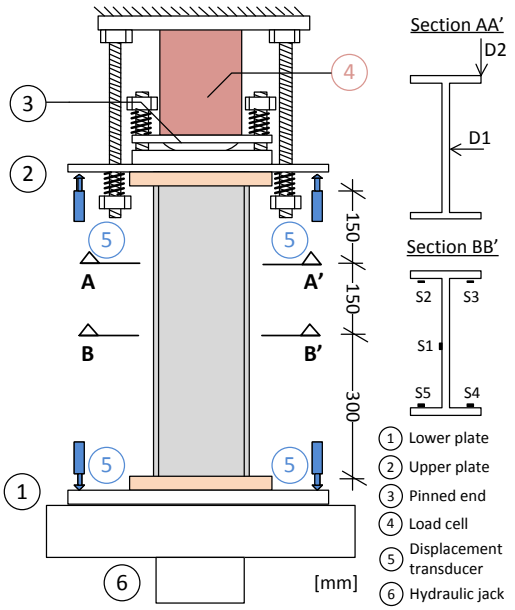

Figure 11 – Short column test schematics with instrumentation.

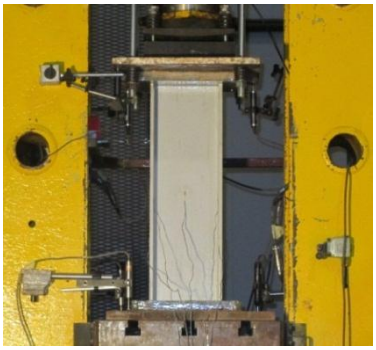

Figure 12 – Short column test setup for column C5

The 450 mm height was chosen for transversal displacement measuring purposes, based on preliminary numerical results that indicated the location of buckled half-wave maximum. Hence, the web's half-width and the flange edge displacements were measured by means of two *TML-50* (50 mm range and 0.01 mm precision) displacement transducers (Section AA' on Figure 11). Strain on the mid-span section of column C5 was measured using five *TML-FLK* strain gages adhesively bonded to the half-width of the column web and the edges interior face of both flanges (Section BB' on Figure 11). Data acquisition was made via *National Instruments SCXI-1001* board and processed on PC, at a rate of 1 Hz. The tests were conducted at an average speed of 50 kN/min.

Figure 13 shows load-axial shortening curves for each column tested. Initial adjustments were corrected in order to obtain effective maximum axial shorting (Δ_{max}) by considering a linear behavior based on displacement data from 200 kN to 400 kN.

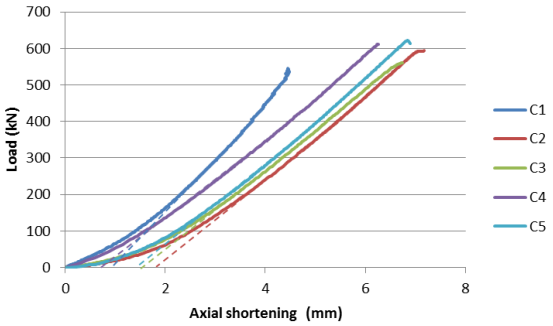

Figure 13 – Load-axial shortening curves obtain for short column testing.

Column C1 was previously tested enabling to confirm the most probable critical buckling mode; hence, no lateral displacement or strain was measured on that column. Figure 14 shows load-lateral displacement curves for columns C2 to C5.

Graphical determination was used to obtain the critical buckling load. Buckling can be seen from lateral displacement data, related with the point at which a sudden slope change occurs in the load-lateral displacement curves. Hence, by extending the initial linear slope and the final linear (post-buckled) slope, the intersection of those curves corresponds approximately to the buckling load.

Table 4 shows buckling and ultimate loads, as well as maximum axial shortening and lateral displacements for each tested column.

Table 4
Buckling (P_{cr}) and ultimate load (P_{max}), axial shortening (Δ_{max}) and lateral displacements ($D1_{max}$ $D2_{max}$) obtained on short column tests.

Column	P_{cr} (kN)	P_{max} (kN)	Δ_{max} (mm)	$D1_{max}$ (mm)	$D2_{max}$ (mm)
C1	-	545.24	3.04	-	-
C2	600	593.37	5.36	2.50	1.00
C3	550	561.32	4.90	7.45	3.74
C4	600	611.86	4.39	2.47	1.53
C5	630	622.24	5.11	2.05	0.98
Average	595.0	597.2*	4.94*	-	-
Deviation	33.3	33.4*	0.41*	-	-
CV (%)	5.6	4.5	8.3	-	-

* excluding column C1 data due to excessive differences.

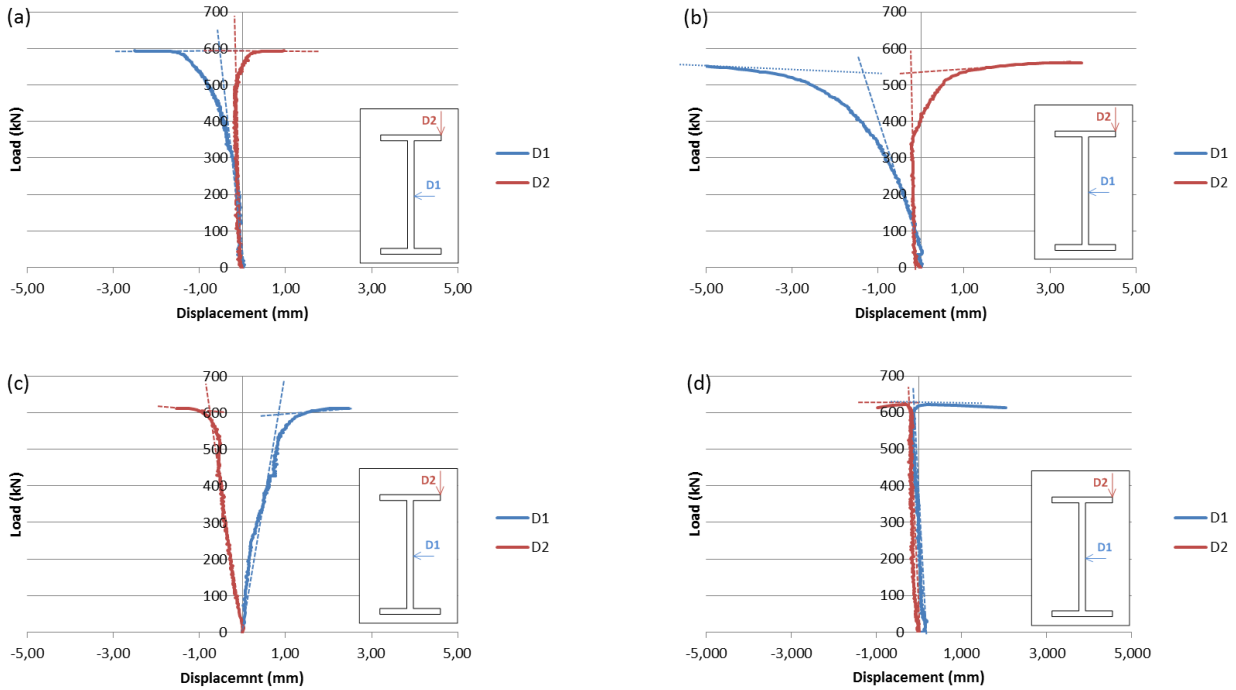

Figure 14 – Load-lateral displacement curves obtain from short column testing: C2 (a), C3 (b), C4 (c) and C5 (d).

The ultimate load obtained from short column tests was 597.2 kN ± 4.5%, with a maximum axial shortening of 4.94 mm ± 8.3%. Those values excluded the column C1 data. The buckling load obtain was 595 kN ± 5.6% due to flange local buckling (P_{max}=*1.004* P_{cr}), with a critical stress on the flanges of 153.4 MPa. Adopting Kollár's analytical method, the critical stress is 118.5 MPa (P_{cr}=*459.7 kN*) and the web governs local buckling. The 30% difference is very significant and it can be explained by: (i) the analytical critical stress was obtained for the web, while the experimental was obtained for the flange; (ii) low transversal elastic modulus (usually 9 GPa); and (iii) Kollár equations do not take into consideration the transversal boundary conditions, which can underestimate the critical stress.

Figure 15 shows the longitudinal stress-strain curves for column C5, measured from the strain gages. It can be seen that local buckling occurs when the linear behavior is suddenly interrupted, changing dramatically its behavior in the post-buckled regime until collapse occurs. According with prior numerical studies, buckling occurred with a two half-wave configuration for all the tested columns. Initially one or both flanges buckled locally; the collapse occurred after 30 cm long cracks appeared in the web-flange junction and the flange material failed. All the columns collapsed due to local buckling of both flanges (Figure 16), except for column C3 that collapsed due to local buckling of only one flange. Such result can be explained by a non-concentrical axial load (Figure 17).

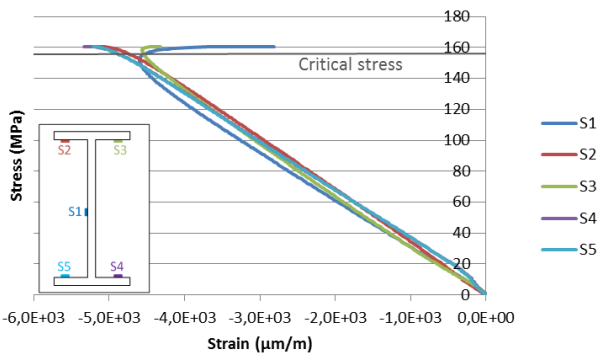

Figure 15 – Longitudinal stress-strain curves for half height section on column C5 testing.

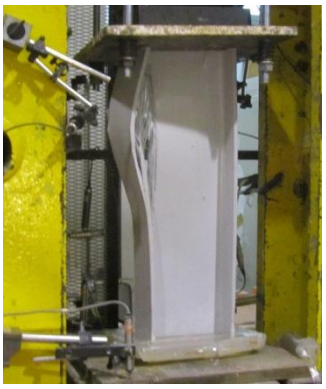

Figure 16 – Column C3 buckled configuration after collapsing.

Figure 17 – Column C5 buckled configuration after collapsing.

4.2. *Three-point bending beam*

In order to obtain flexural and shear moduli, the EN 13706 Annex G method [11] was followed. Thus, a simply supported beam was tested for different span lengths (*L*): 1.40 m, 2.10 m, 2.80 m and 3.50 m).

Due to typical low shear-to-elastic flexural moduli ratio, also called *anisotropy degree*, the determination of elastic moduli at a full-section level, both should consider the flexural deformation and shear deformation. Thus, the Timoshenko Beam Theory (TBT) should be considered instead of the Euler-Bernoulli Theory (EBT). The mid-span deflection for a three-point bending beam is given by:

$$\delta = \frac{PL}{4GkA_V} + \frac{1}{48}\frac{PL}{EI} \tag{9}$$

As the TBT was considered, flexural and shear moduli are named "effective". On the other hand, if the EBT was considered, flexural modulus is named "apparent" [12] and is given by:

$$\frac{1}{E_a} = \frac{1}{E}\left(1 + 12\frac{E/_{kG}}{\lambda^2}\right) \tag{10}$$

Figure 19 shows the testing schematics used on three-point bending beam tests, and Figure 20 shows the test setup.

The load (*P*) was applied at mid-span on the superior flange of the profile by a *Enerpac* hydraulic jack with 600 kN load capacity and a maximum stroke of 250 mm; it was measured by means of a *Novatech* load cell with 100 kN capacity. The deflection at the mid-span (δ) was measured by a *TML-100* displacement transducer, of 100 mm range and 0.01 mm precision. Data acquisition was made via *HBM Spider8* board and processed on PC, at a rate of 10 Hz.

Roberts and Al-Ubaidi [13] suggest that shear stiffness and shear modulus show significant variation when determined by full-scale beam tests. Hence, two load cycles were performed on each span length tested; due to GFRP linear elastic behavior monotonic load was applied up to 5 kN, and then unloaded. Prior numerical studies for three-point bending were developed in order to prevent lateral-torsional buckling ($P > 14.39$ *kN*). The tests were conducted at an average speed of 5 kN/min.

Flexural and shear stiffnesses can be obtain by plotting the results for each span as δ/PL-L^2 (Figure 18) and δ /PL^3-$1/L^2$ (Figure 21) according with Method A of EN 13706 for flexural and shear stiffness properties. Thus, the flexural stiffness can be obtain from the slope on Figure 18, and the shear stiffness can be obtain from the slope of results depicted in Figure 21. As a cross-check measure, intersection of the strength line with the y-axis in Figure 18 should agree with that of Figure 21, and vice-versa.

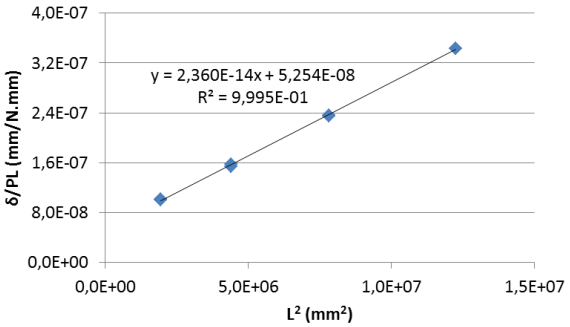

Figure 18 – Plot of δ/PL versus L^2 for three-point bending beam flexural and shear stiffnesses determination.

The flexural and shear effective moduli obtained were 37.39 GPa and 2.87 GPa, respectively, with an anisotropy ratio of 13.0. An expected 12% influence of shear deformation on total deflection was obtained for a span length of 4.4 m given by:

$$L_{12\%} = \sqrt{\frac{100\ EI}{GkA_v}} \tag{11}$$

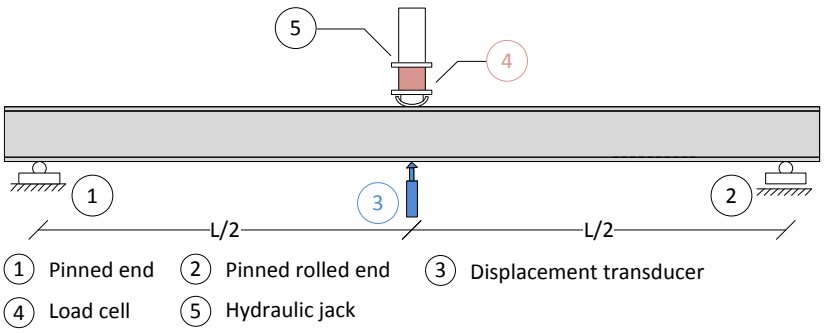

Figure 19 – Three-point bending beam test schematics with instrumentation.

Figure 20 –Three-point bending beam test setup.

Thus, for the range of span lengths tested the influence of shear deformation on the total beam deflection was higher than 12%.

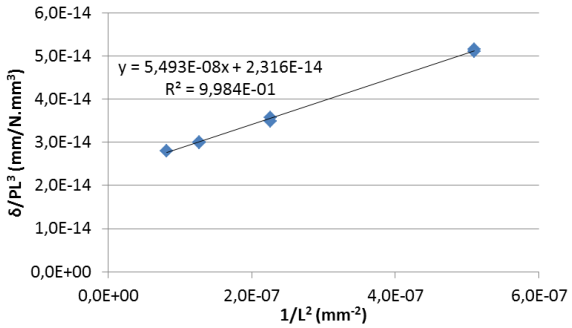

Figure 21 – Plot of δ/PL^3 versus $1/L^2$ for three-point bending beam flexural and shear stiffnesses determination.

4.3. *Four-point bending beam*

The main goal of this test was to obtain the buckling and ultimate load for four-point bending. The beam tested was simply supported with a 4.0 m span length; the load was applied 1.3 m from each support. As referred previously for the three-point bending test, TBT should be considered in order to predict the deflection of the beam considering the shear deformation. The (symmetrical) deflection (in m) of the beam, function of the distance (x) to the pinned end, is given by:

$$\delta(x) = \begin{cases} \dfrac{Px}{2GkA_v} + \dfrac{Px}{4EI}\left(3.51 - \dfrac{x^2}{3}\right), x \in [0.0; 1.3] \\ \dfrac{1.3\,P}{2GkA_v} + \dfrac{1.3\,P}{4EI}(4x - x^2 - 563.3), x \in [1.3; 2.0] \end{cases} \quad (12)$$

Figure 22 shows the scheme used for the four-point bending test. Figure 23 shows a schematic detail of the load application system and Figure 24 shows the four-point bending beam test setup.

In order to apply the same load on two points, the load was applied at mid-span on an auxiliary steel beam, with stiffness and strength properties that enabled a correct load transfer to the tested beam. The auxiliary beam was transferred the load to two steel rollers located over the superior flange of the profile. The load was applied by a *Enerpac* hydraulic jack with 600 kN load capacity and a maximum stroke of 250 mm; it was measured by means of a *Novatech* load cell with 100 kN capacity.

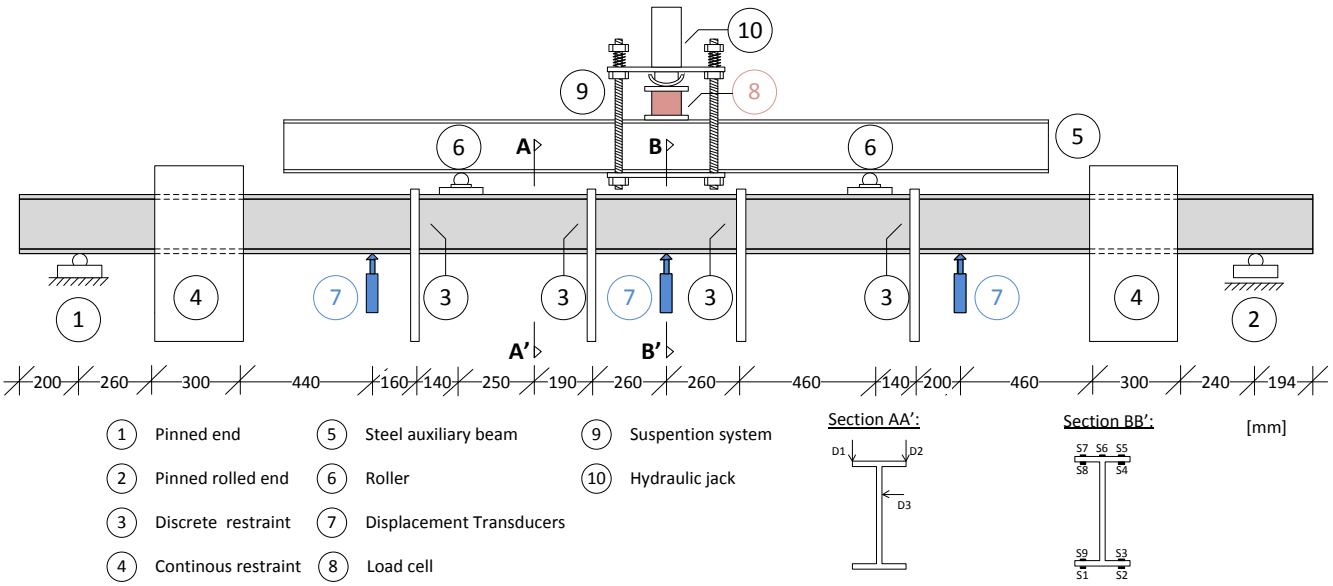

Figure 22 – Four-point bending beam test schematics with instrumentation.

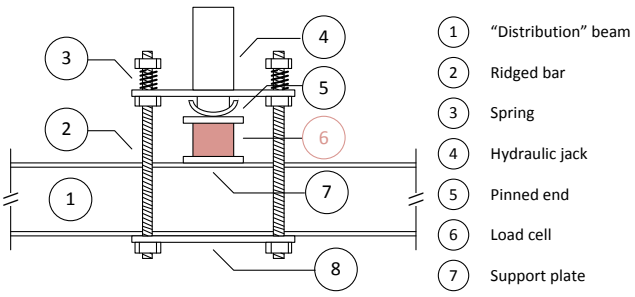

Figure 23 – Load application system on the four-point bending beam testing schematic detail.

Figure 24 – Four-point bending beam test setup.

The deflection was measured in three point spaced 1.0 m from each other: at 1.0 m from each support (*d1* and *d3*) the displacements were measured by means of two *TML-100* displacement transducer (100 mm range and 0.01 mm precision), and at the mid-span (*d2*) it was measured by a *APEK-100* displacement transducer (100 mm range and 0.01 mm precision). A section located 1550 mm from the pinned end was chosen for transversal displacement measuring purposes, based on prior numerical tests indicating where the buckled half-wave maximum would occur. In both edges of the top flange, vertical displacements were measured and the lateral displacement of the web ¾ width by means of three *TML-500* (500 mm range and 0.01 mm precision) displacement transducers (Section AA' on Figure 22). Strain in the mid-span section was measured by nine *TML-FLK* strain gages adhesively bonded to the half-width of the web, to the edges of both flanges on the interior and exterior faces, and to the center of the top flange on the external face (Section BB' on Figure 22). Data acquisition was made via *HBM Spider8* data logger and processed on PC, at a rate of 10 Hz. The test was conducted at an average speed of 5 kN/min. In order to prevent the beam from buckling laterally, eight steel props were placed against the profile on each side; torsion on the supports was prevented by four steel triangular blocks, one on each side of both supports. The load was applied until the beam collapsed.

Figure 25 shows the deflections, spaced by 1.0 m from each other plotted, versus the load. Linear elastic behavior can be seen until the beam collapses at 61.3 kN, corresponding to a maximum bending moment of 39.7 kNm. The maximum displacement obtained was at the mid-span (*d2*) and it was 85.26 mm; *d1* maximum value was 63.08 and *d3* maximum value was 61.67 mm.

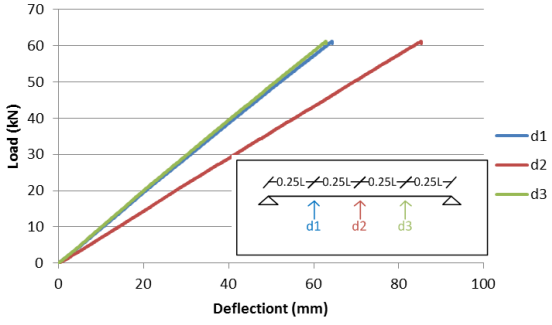

Figure 25 – Load-deflection curves at one meter from each support and at mid-span for the four-point bending beam test.

By averaging the strain measured by the strain gages located on the face of both flanges, linear elastic behavior can also be seen, as it is shown in Figure 26. *SD* strain gages disabled during the test, before the collapse occurred. Hence, strain data for loads higher than 40 kN were not measured. Strain data for the top flange, comparing with the bottom one, indicate that it may have buckled locally due to compression. Thus, the strain measured in the top flange was plotted versus the bending moment (see Figure 27). The observed divergent strains indicate that local buckling of the top flange occurred when the maximum bending moment is reached.

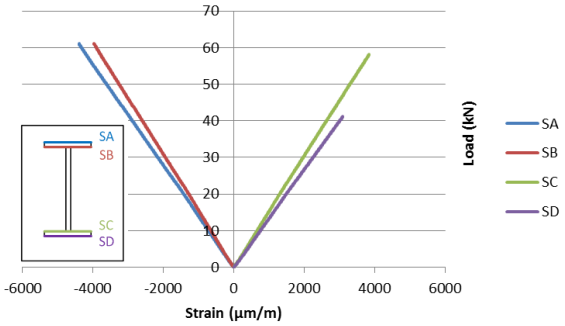

Figure 26 – Load-average strain curves at mid-span on both flanges for the four-point bending beam test.

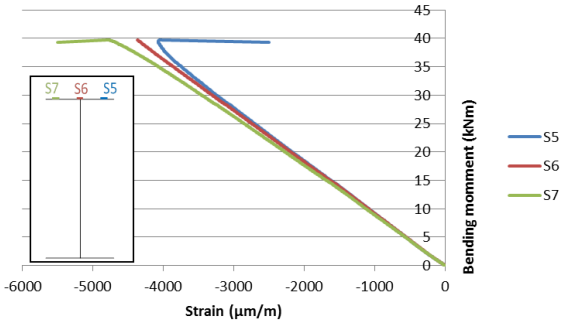

Figure 27 – Bending moment-strain curves on the top flange at mid-span for four-point bending beam test.

Figure 28 shows the load versus vertical displacement in the top flange measured in section AA' (Figure 22). The displacement transducer D3 obtained improper data results due to the bad connection to the data logger, hence it was not considered. For loads higher than approximately 55 kN, a small divergence can be seen. Therefore, the difference between those displacements was plotted versus the load, as shown on Figure 29. Buckling is related with the point at which a sudden slope change occurs on load-displacement curve. Thus, by plotting a linear regression for the initial slope and for the final linear (post-buckled) slope, the intersection of those curves is the buckling load, approximately 55 kN, corresponding to a bending moment of 35.80 kNm and a critical stress in the top flange of 152.2 MPa. However, due to the fact that the vertical displacements of the top flange were measured near the inflection point between two half-waves, the buckling load may have been misinterpreted.

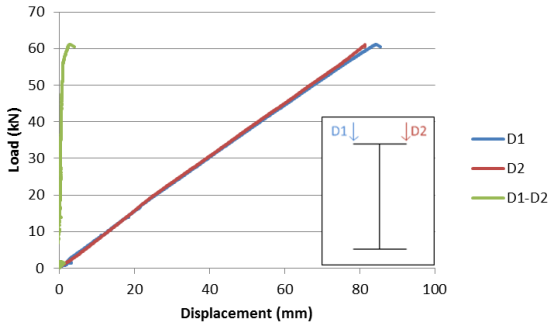

Figure 28 – Load-vertical displacement curves on the top flange at section AA' for the four-point bending beam test.

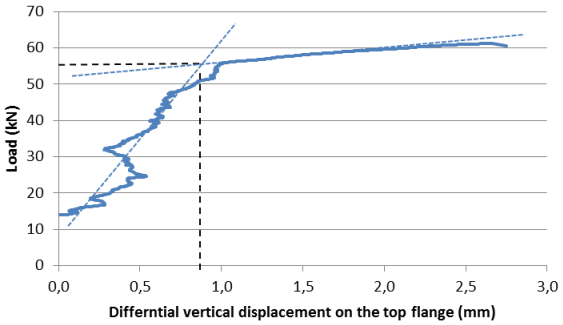

Figure 29 – Load-differential vertical displacement curve on the top flange at section AA' for four-point bending beam test.

Strain data for incremental values of bending moment are plotted along the web height (Figure 30). The uniform evolution of those strains, obtaining zero strain at the center of gravity, suggests that the section was kept plane at mid-span, implying that the EBT may be considered on this beam segment, in other words, shear deformation can be neglected. Hence, the flexural effective modulus was obtained by plotting the curvature at mid-span versus the bending moment as shown on Figure 31, considering that shear deformation had no influence. A 37.93 GPa flexural modulus was obtained, similar to the one obtained from the three-point bending tests (-1%).

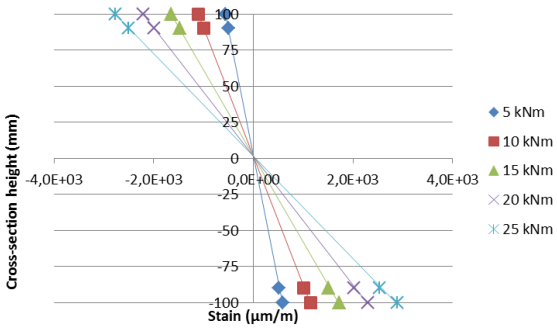

Figure 30 – Evolution of strain data for incremental values of bending moment on the cross-section height.

Adopting Kollár's analytical method, the critical stress in the compressed flange was 159.8 MPa, leading to a 39.4 kNm bending moment. This value is lower than the one obtained experimentally. Such difference (-10%) can be explained by the fact that material transverse failure occurred at the web-flange junction, followed by immediate buckling of the top flange that lowered its critical stress to 29.4 MPa.

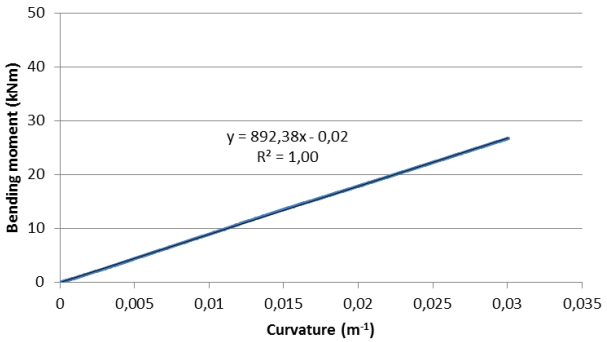

Figure 31 – Bending moment-curvature curve at the mid-span section for the four-point bending beam.

Figure 32 shows the buckled four-point bending beam top flange. It can be seen that the web-flange junction was crushed, triggering the flange buckling.

Figure 32 – Four-point bending beam buckled configuration after collapsing.

5. NUMERICAL MODELLING

The finite element method (FEM) using *Abaqus* software was applied in order to model the short columns and the four-point bending beam, and to analyze their local buckling susceptibility. Those models were calibrated based on the experimental data obtained from coupon and full-scale tests in order to perform parametric studies with different cross-section shapes and span lengths.

Linear buckling analysis was conducted in order to obtain the buckling load (P_{cr}) and the buckling mode configuration. Then, a nonlinear analysis was performed in order to obtain the ultimate load (P_u) of the model, using Tsai-Wu failure criterion.

A 23-noded generic cross-section was defined in order to generate four-noded rectangular shell elements that were used to model the short column and the beam. The element strength properties were considered to be those

obtained from coupon tests, and the stiffness properties were considered to be those obtained from short column and three-point bending beam full-scale tests.

In these numerical studies, progressive failure of the members was not considered due to the complexity of the process and absence of available procedures in Abaqus to take into account these effects. Hence, the ultimate load/stress was considered to be the one related with the first point to exceed the failure index of Tsai-Wu, given by:

$$I_F = \frac{\sigma_{11}^2}{\sigma_{u,x}^2} + \left(\frac{1}{F_{SBS}^2} + 2F_{12}\right)\tau_{12}^2 + \frac{\sigma_{22}^2}{\sigma_{u,y}^2} \leq 1{,}0 \qquad (13)$$

where σ_{11} is the stress in direction 1, σ_{22} is the stress in direction 2, τ_{12} is the shear stress and F_{12} is given by:

$$F_{12} = \frac{1}{2}\sqrt{\frac{1}{\sigma_{cu,x}\sigma_{tu,x}\sigma_{cu,y}\sigma_{tu,y}}} \qquad (14)$$

5.1. *Short column model*

The short column was modeled with 660 elements and the aspect ratio of the finite elements was 2:1, sufficiently small in order to not affect the calculations accuracy. To simulate the column supports, both ends were restrained at the profile centroid by rigid shell elements. Both ends were totally restrained, except for the *v* displacement (in y direction) at the top end section. A concentric load was applied to the top end centroid, as shown on Figure 33.

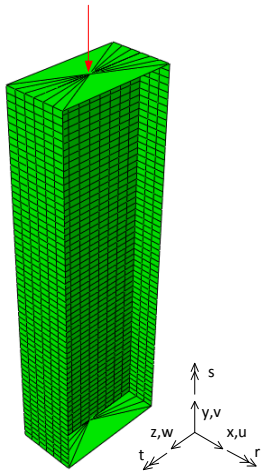

Figure 33 – Short column numerical model

The buckling load obtained from the linear buckling analysis was 531.77 kN, associated to a local buckling configuration with two half-waves. Figure 34 shows the buckling mode for the short column model.

The nonlinear analysis aimed to predict the pre- and post-buckling responses. Based on the buckling mode obtained from the previous analysis, a 0.1 mm imperfection was considered.

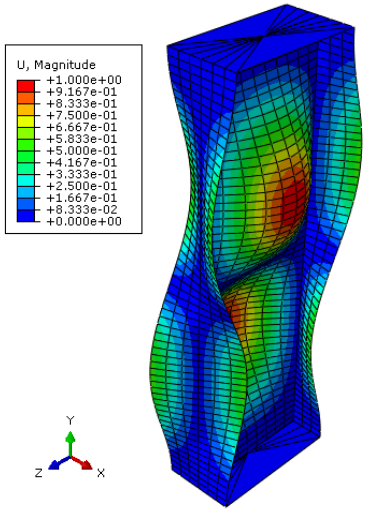

Figure 34 – Short column model's buckling mode.

Following the procedure used by Turvey and Zhang [2] to analyze postbuckling of columns, small load steps were considered to analyze variation of the top and bottom surface longitudinal stress (Figure 35) and shear stress (Figure 36) along the finite elements located along the web-flange junction.

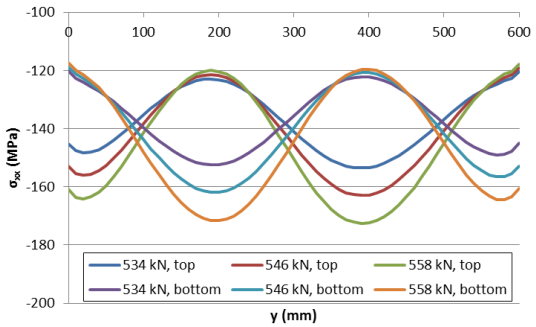

Figure 35 – Postbuckled surface longitudinal stress along the web-flange junction.

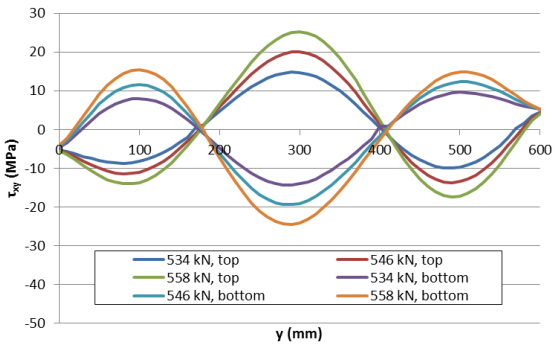

Figure 36 – Postbuckled surface shear stress along the web-flange junction.

The constant variation on both stresses along the web-flange junction suggests that no mode change occurred. Thus, failure index for Tsai-Wu criterion ($I_{F,Tsai\text{-}Wu}$) was used to the web-flange junction elements.

Figure 37 shows the load-axial shortening curve for the nonlinear analysis of short column model. The unit failure index was exceeded for a axial shortening of 2.79 mm corresponding to a ultimate load of 562.85 kN. The nodes in failure were located at the half height of the column, in both web-flange junctions.

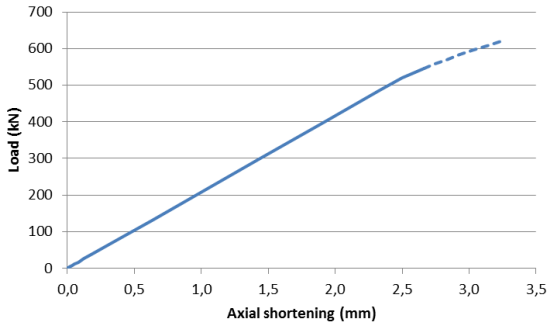

Figure 37 – Load-axial shortening curve for the short column model nonlinear analysis.

Lateral displacement data for the numerical model were plotted versus the load, as shown on Figure 38.

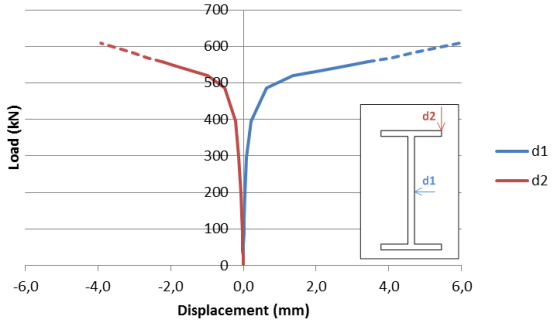

Figure 38 – Load-lateral displacement curves for the short column nonlinear analysis.

The shear stress in the nodes that first exceeded the failure index was 90% of the material interlaminar shear resistance, thus contributing the most for the web-flange junction failure.

Calibration was performed based on the change of the elastic moduli and measuring their influence on the axial shortening, buckling load and ultimate load. The calibration of the elastic moduli is shown on Table 5.

Relative differences between the calibrated model and the experimental results were below 0.5%. Axial shortening was 4.41 mm, the buckling load was 615.12 kN and the ultimate load was 624.19 kN. However, the elastic moduli were remarkably changed (roughly 50%): one increased and the other two decreased. This fact can be explained by: (i) the relative independence of the behavior parameters from the elastic moduli; (ii) having considered a 600 mm column length instead of 660 mm, the total length including the part confined by the epoxy resin blocks; (iii) dependency of the elastic moduli on the resin used to produce GFRP; (iv) low E_{yy} value comparing with usual values; and (v) the possible (most likely) material crushing on the ends of the column.

Table 5
Elastic moduli calibration for the short column model.

Model	E_{xx} (GPa)		E_{yy} (GPa)		G_{xy} (GPa)	
	Value	Dif.	Value	Dif.	Value	Dif.
Initial	31.95	-	5.03	-	3.67	-
Calibrated	17.30	-45.9%	10.0	98.8%	5.50	49.9%

Figure 39 shows the experimental and calibrated results for the load-axial shortening curves. The lateral displacement was calibrated with the imperfection. A 0.021 mm value was considered due to the Abaqus limitation on choosing the minimum value. Figure 40 shows load- lateral displacement curves for experimental and calibrated results.

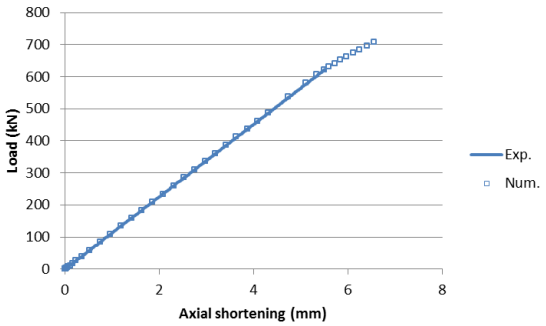

Figure 39 – Load-axial shortening curve for experimental and calibrated results for the short column model.

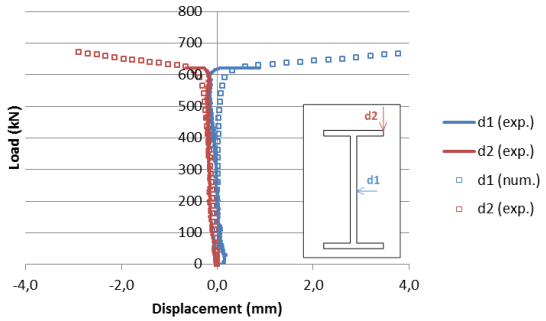

Figure 40 – Load-lateral displacement for experimental and calibrated results for the short column model.

Parametric studies were conducted for different column span lengths (from 300 mm to 4000 mm). Two cross-sections were considered, the "I" section and a "H" section with a flange width equal to the web depth. Figure 41 shows the buckling load versus the span length.

The "I" cross-section is more susceptible to global buckling due to its lower inertia about the minor axis, comparing with the "H" cross-section. On the other hand, the "H"

cross-section is more sensitive to local buckling due to the fact that its flanges are wider, and so more sensitive to local buckling than "I" cross-section columns.

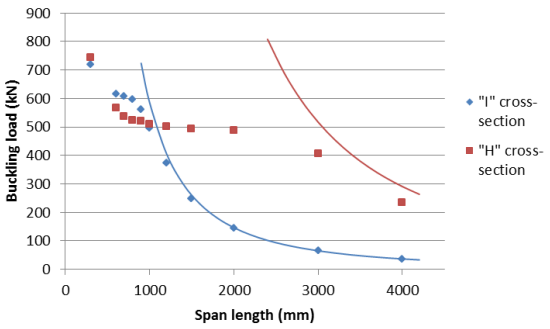

Figure 41 – Buckling load for different span length for "I" and "H" sections.

5.2. Four-point bending beam model

The beam was modeled with 2420 elements and the aspect ratio of the finite elements was 1:2, sufficiently small not to affect the calculations' accuracy. To simulate the beam supports, the nodes of the lower flange, located at 200 mm from both ends (five elements), were restrained for the *u* and *v* displacements (in x and y directions) and *s* and *t* rotations (in y and z directions). The left support also restrained the *w* displacement (in z direction). To model the local restraints (Figure 22), the web-flange junction nodes had their *u* displacement blocked, in order to avoid local crushing on the transversal material direction of the flanges. The web-top flange junction nodes in the support section had also their *u* displacement restrained.

The load was applied at approximately 1/3 and 2/3 of the span length by means of 10 concentrated loads (five on each side) applied on the web-top flange junction. Figure 43 shows the boundary conditions and loading of the beam model.

The buckling load obtained from the linear buckling analysis was 80.80 kN for a local buckling configuration with six half-waves. It corresponds to a 57.72 kNm maximum bending moment. Figure 44 shows the buckling mode for the four-point bending beam model.

The nonlinear analysis aimed to predict the pre- and post-buckling responses. Unlike the short column model, the imperfection sensitivity should be studied before the performance of nonlinear analysis. Thus, several values of initial imperfection were tested in order to find the one that would fit better its behavior to the experimental results. Figure 42 plots the differential vertical displacement of the top flange edges at section AA' (Figure 22) versus the load, for different values of imperfection and the experimental results.

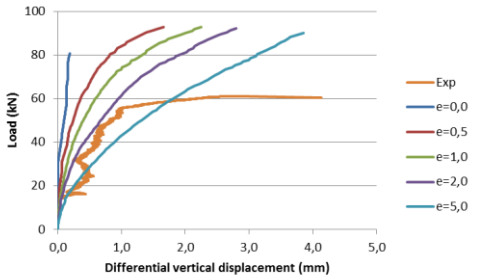

Figure 42 – Load-differential vertical displacement of the top flange experimental and numerical curves.

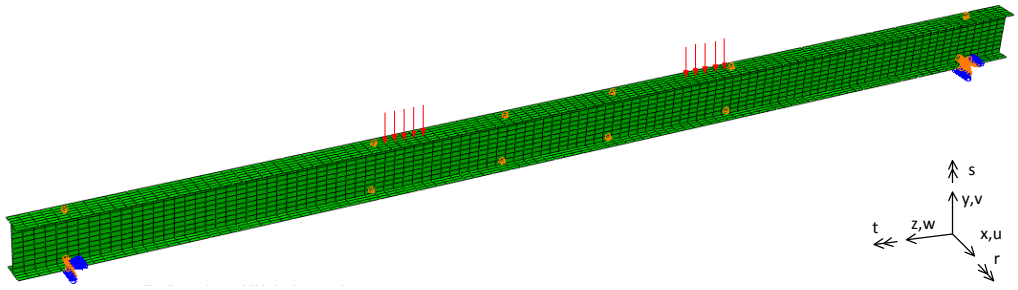

Figure 43 – Four-point bending beam numerical model.

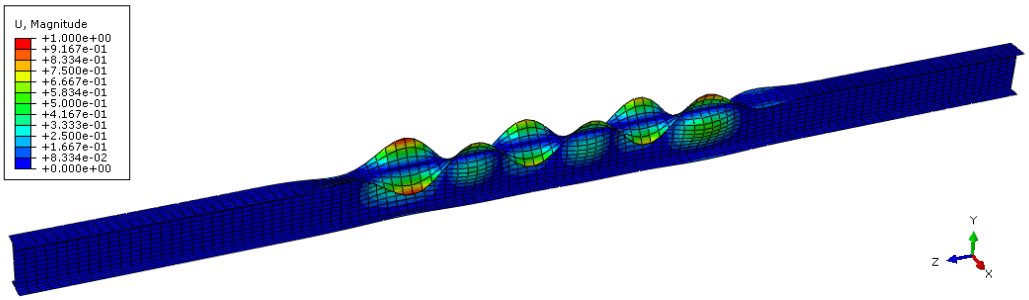

Figure 44 – Four-point bending beam model's buckling mode

Therefore, a buckling mode shape imperfection with a 2.0 mm amplitude was included in the nonlinear analysis.

Figure 45 shows the load-deflection curves of the beam model. The unit failure criterion (Tsai-Wu) was exceeded for a load level lower than the buckling load (62.79 kN). In other words, the beam collapsed before it buckled, as it was seen during the experimental test.

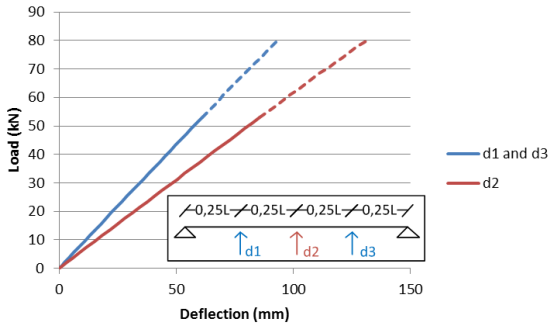

Figure 45 – Load-deflection curves for the four-point bending beam model nonlinear analysis.

Figure 46 shows the differential vertical displacement of the top flange edges versus the load.

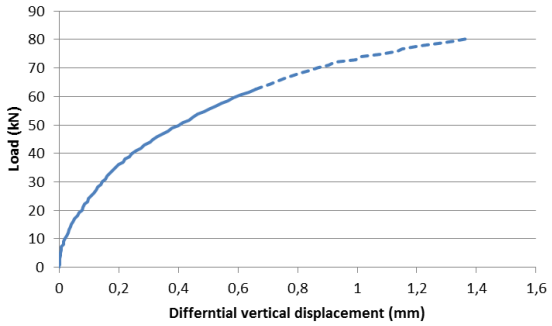

Figure 46 – Load-differential vertical displacement curve for the four-point bending beam model nonlinear analysis.

Calibration was performed based on the change of the elastic moduli at a first stage, and measuring their influence on the mid-span deflection. The calibration of elastic moduli is shown in Table 6.

Table 6
Elastic moduli calibration for the beam model.

Model	E_{xx} (GPa)		E_{yy} (GPa)		G_{xy} (GPa)	
	Value	Dif.	Value	Dif.	Value	Dif.
Initial	37.39	-	5.03	-	2.87	-
Calibrated	45.00	20.4%	5.03	0.0%	3.67	27.9%

The deflection at the mid-span section for the calibrated model was 84.40 mm, less than 1% error comparing with experimental data. For the experimental load corresponding to the collapse, the calibrated model already had 13 nodes exceeding the Tsai-Wu unit failure index. Hence, strength properties were also calibrated in order to match the ultimate load of the calibrated model and the experimental beam results. Transversal tensile strength ($\sigma_{tu,y}$) and interlaminar shear strength (F_{SBS}) were calibrated to 80.27 MPa (+45.9%) and 38.00 MPa (+27.5%), respectively. Figure 47 shows deflection versus load results for experimental and calibrated results.

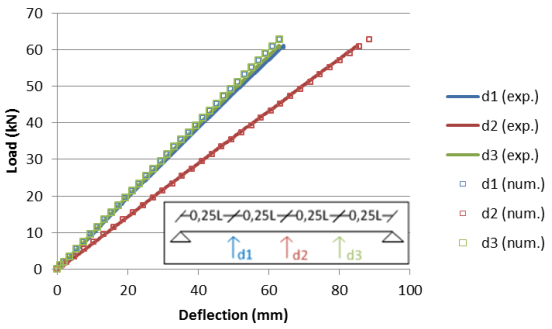

Figure 47 – Load-deflection curves for experimental and calibrated results for the four-point bending beam model.

In order to calibrate the differential vertical displacement of section AA', the imperfection was changed to 5.0 mm, as shown on Figure 48.

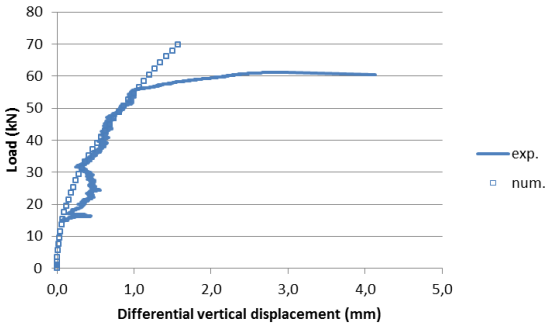

Figure 48 – Load-differential vertical displacement on the top flange for experimental and calibrated results for the four-point bending beam model.

Cross-section shape sensitivity was studied comparing the "I" with a "H" cross-section. The buckling load for the "I" shape (104.97 kN) was twice that for the "H" cross-section (55.55 kN). This can be explained by the wider flanges of the "H" shape. Thus, this cross-section may allow to experimentally observing elastic local buckling mode easier than with an "I" cross-section.

6. CONCLUSIONS

This dissertation provided a better knowledge about GFRP general structural behavior, namely deflections (SLS) and local buckling (ULS) of columns and beams.

Mechanical properties obtained from experimental coupon tests were consistent with the manufacturer data. Short column full-scale tests enabled to observe local buckling. On the other hand, the four-point bending beam test showed one of the major disadvantages of GFRP, the transversal material strength. The beam material failed before local buckling occurred.

Numerical models predicted accurately GFRP member behavior, namely the buckling mode shape. Calibrated models enabled to understand "I" profiles general greater sensitivity to global buckling and that "H" profiles are more sensitive to local buckling.

The results obtained in this dissertation should be compared with those obtained by Francisco Nunes [15] in order to compare the influence of CFRP (Carbon Fiber Reinforced Polymers) strip in the deflection and local buckling of GFRP pultruded profiles.

7. REFERENCES

[1] BANK, L. C., e YIN, J. (1999), Failure of Web-Flange Junction in Postbubkled pultrud I-Beams, *Journal of Composites for Construction*, Vol. 3, No. 4, pp. 177-184;

[2] TURVEY, G. J. e ZHANG, Y. (2006), A computational and experimental analysis of the buckling, postbuckling and initial failure of pultruded GRP columns, *Computers and Structures*, Vol. 84, pp. 1527-1537;

[3] KOLLÁR, L.P. (2002), Buckling of unidirectionally loaded composite plates with one free and one rotationally restrained unloaded edge, *Journal of Structural Engineering*, Vol. 128, No. 9, pp. 1202-1211;

[4] KOLLÁR, L. P. (2003), Local buckling of fiber reinforced plastic composite structural members with open and closes cross-section, *Journal of Structural Engineering*, Vol. 129, No. 11, pp. 1503-1513;

[5] ASTM International (2002), *Standard Test Method for Compressive Properties of Rigid Plastics (D 695)*, West Conshohocken, Pennsylvania;

[6] Comité Européen de Normalisation (1997), *Plastiques – Détermination des propriétés en traction (ISO 527:1997)*, Brussels;

[7] Comité Européen de Normalisation (1998), *Fiber-reinforced plastic composites: determination of flexural properties (ISO 14125:1998)*, Brussels;

[8] ASTM International (2000), *Standard Test Method for Short-Beam Strength of Polymer Matrix Composite Materials and their Laminates (D 2344)*, West Conshohocken, Pennsylvania;

[9] HODGKINSON, J.M. (2000), *Mechanical Testing of Advanced Fiber Composites*, CRC Press, Boca Raton, California;

[10] BANK L. C. (2006), *Composites for Construction: Structural design with FRP materials*, John Wiley & sons, New York;

[11] Comité Européen de Normalisation (2002), *Reinforced plastics composites: specifications for pultruded profiles (EN 13706:2002)*, Brussels;

[12] BANK, L. C. (1989), Flexural and shear moduli of full-section Fiber Reinforced plastic (FRP) pultruded beams, *Journal of Testing and Evaluation*, Vol. 17, No. 1, pp. 40-45;

[13] ROBERTS, T. M., AL-UBAIDI, H. (2002), Flexural and torsional properties of pultruded fiber reinforced plastic I-profiles, *Journal of Composites for Constructions*, Vol. 6, No. 1, pp. 28-34;

[14] Abaqus CAE 6.10 (2010), Simulia;

[15] NUNES, F. (2012), *Structural behavior of GFRP pultruded profiles reinforced with CFRP strips: experimental characterization and numerical modeling*, Masters of Science Civil Engineering Dissertation, Instituto Superior Técnico, Universidade Técnica de Lisboa, Lisbon.